Mechanical Enhancement of the Strain-Sensor Response in Dimers of Strongly Coupled Plasmonic Nanoparticles

Najat Ahmidayi, William d'Orsonnens, Thomas Maurer, Gaëtan Lévêque

annalen der physik
www.ann-phys.org

Mechanical Enhancement of the Strain-Sensor Response in Dimers of Strongly Coupled Plasmonic Nanoparticles

Najat Ahmidayi, William d'Orsonnens, Thomas Maurer, and Gaëtan Lévêque**

Due to their particular optical and mechanical properties, plasmomechanical devices have become choice candidates in strain sensing applications. Using numerical simulation, a plasmomechanical system consisting of two gold nanoparticles with different shapes and separated by a small gap, deposited onto a deformable polydimethylsiloxane membrane, is investigated. With the aim of understanding the relationship between the plasmonic behavior of gold nanoparticles and induced mechanical deformations, mechanical extension ranging from 0% to 20% is applied to the polydimethylsiloxane membrane. In a first step, a mechanical calculation based on a hyperelastic model for polydimethylsiloxane shows that the interparticle spacing is enhanced nonlinearly by a percentage greater than the externally applied deformation, depending on the shape and size of the nanoparticles as well as the polydimethylsiloxane membrane thickness. Full optical simulation of the deformed nanosystems demonstrates that the plasmonic resonance wavelength is highly sensitive to the applied displacements and is enhanced compared to a basic approach where the gap deformation is taken as equal to the macroscopic applied deformation. The best figure of merit ($0.022\%^{-1}$) is obtained for the disk–rod dimer near the strong coupling regime, larger than the values reported in the literature for localized nanoparticle systems.

1. Introduction

The capability of metallic nanoparticles (MNPs) to support, through the interaction between their conduction electrons and incident light, localized surface plasmon resonances (LSPR) has made them choice candidates in many applications, such as biosensing,[1] photothermal processes,[2,3] and photovoltaics.[4,5] The plasmonic response of MNPs can be controlled by several parameters, such as the size,[6] shape,[7] material composition, and refractive index of the surrounding medium.[8,9] In addition, in assembled MNPs consisting of two nanoparticles (NPs) or more, the LSPR shows a high sensibility to the interparticle spacing due to the strong coupling via their near-fields.[10–12] Thus, interparticle gap variations may induce large shifts in the resonance frequency of LSPRs. Hence, the possibility of measuring the interparticle spacing with nanometric precision from the optical response of nanostructures has been proposed.[13] This fascinating property has paved the way for the birth of plasmomechanics[14] as a new field of nanophotonics.

Plasmomechanical systems are composed of metallic nanostructures supported by, or embedded in, a flexible membrane, such as polymers. Under mechanical strains, changes in the interparticle separations and distribution of MNPs composing the plasmomechanical system may occur, which translate into changes in their plasmon colors in the visible range,[15] in their electric conductivity under a change in the applied pressure,[16] or in the generated heat in the gap region.[17–19] Therefore, those systems are crucial in thermoplasmonic and strain-sensing applications. In this context, several systems, based on disordered assemblies,[20] periodic[21,22] arrays, and isolated NP dimers,[23,24] have been proposed. Most of them use polydimethylsiloxane (PDMS) as a membrane due to its unique flexibility. However, to well understand the plasmonic behavior of those systems, it is necessary to know how the interparticle gap is affected by an applied macroscopic strain, in relation with the geometrical parameters of the membrane and the particles, including their shape and size. In literature, it is generally supposed that the interparticle gap deforms as equal to the macroscopic applied deformation.[18,25] However, this basic assumption contradicts previous experimental findings.[22,23] To the best of our knowledge, this is the first time that the real evolution of the interparticle gap has been numerically studied.

The realization of strain sensors with high performance requires plasmonic resonances with a high-quality factor, such as Fano resonances (FR).[26,27] Rod-shaped NPs are known to support plasmonic large bright and narrow dark modes alternating

N. Ahmidayi, G. Lévêque
Institut d'Electronique
Microélectronique et Nanotechnologie, UMR CNRS 8520
Université de Lille
Villeneuve d'Ascq 59652, France
E-mail: najat.ahmidayi@univ-lille.fr; gaetan.leveque@univ-lille.fr
W. d'Orsonnens, T. Maurer
Laboratory Light, Nanomaterials and Nanotechnologies–L2n
University of Technology of Troyes and CNRS EMR 7004
12 rue Marie Curie, CS 42060, CEDEX
Troyes 10004, France

The ORCID identification number(s) for the author(s) of this article can be found under https://doi.org/10.1002/andp.202300319

DOI: 10.1002/andp.202300319

in frequencies.[28] Those dark modes can be used, when the environment of the nanorod is broken using other particles as other nanorods[29] or nanodisks,[30] supporting bright modes, to generate FR whose profile can be modified by the deformation of a PDMS membrane.

Herein, a detailed numerical study of different plasmomechanical systems is proposed. First, mechanical simulations are realized for applied deformations up to 20%, where PDMS is described using a hyperelastic model. We characterize the evolution of the gap with the applied deformation, together with the geometrical parameters of the PDMS membrane. We compare the results with a simplified approach where the gap is supposed to evolve following the applied deformation. The study of the effect of these geometrical parameters is crucial to understand the plasmonic response of the plasmomechanical systems under strain. Finally, an optomechanical simulation of LSPR-(disks dimer) and FR-based (disk–rod system) plasmomechanical systems is performed, and the performances of the devices in terms of sensitivity and figure of merit are extracted and compared to the literature.

2. Model and Numerical Simulation

All numerical simulations were performed using the Comsol Multiphysics software based on the finite element method. In these simulations, the Solid Mechanics module, Radio Frequency module, and Moving Mesh interfaces were utilized. The investigated structure, as schematically shown in **Figure 1**a, consists of two gold NPs (AuNPs) with different shapes deposited on top of a PDMS membrane without being embedded within it, with length L equal to its width and thickness H. All AuNPs have rounded edges of 5 nm, a fixed thickness $h = 30$ nm, and are initially separated by a gap g_0. We investigate four systems in this work: a disks dimer (R denotes the radius, Figure 1b), a squares dimer (l_s denotes the side, Figure 1c), a disk–square system (Figure 1d), and a system of a nanorod (l_r denotes the length and w denotes the width) coupled to a nanodisk with a radius R (Figure 1e). In the first part of the study, a mechanical calculation is done using the Solid Mechanics module in order to understand how the geometrical parameters of the membrane and the AuNPs influence the gap evolution when the system is stretched, considering only the three first dimers (Figure 1b–d). The PDMS membrane was modeled as a nearly incompressible hyperelastic material using the Neo-Hookean model, while the AuNPs are modeled as elastic materials. The mechanical properties of PDMS and gold are reported in **Table 1**.[31,32] To simulate the stretching, faces labeled 1 and 2 on Figure 1a were displaced along the x-axis, respectively, by $\varepsilon L/2$ and $-\varepsilon L/2$, corresponding to a total deformation ε ranging from 0% to 20%. The gap value was measured after each stretch. The second part is devoted to an optomechanical calculation of only two systems: the disks dimer (Figure 1b) and the disk–rod dimer (Figure 1e). The AuNPs are deposited on the PDMS membrane with dimensions $L = 1000$ nm and $H = 300$ nm. The Solid Mechanics and the Radio Frequency modules were combined via the Moving Mesh interface in order to follow the evolution of the plasmonic response of the gold nanostructures during the membrane deformation. The applied displacements are the same as in the previous part. The nanostructures are excited by a monochromatic

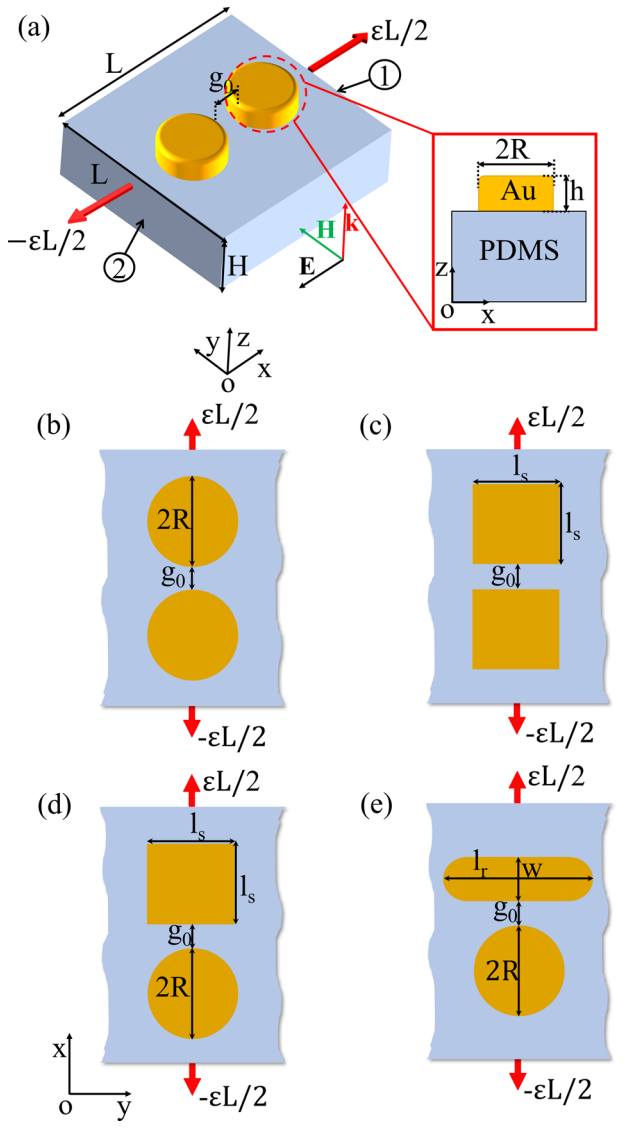

Figure 1. Schematic illustration of the investigated devices: a) Overview and cross-sectional view of the disks dimer system; top view of: b) the disks dimer with radius R; c) the squares dimer with side l_s; d) the square–disk dimer; e) the disk–rod dimer.

plane wave, polarized along the x-axis and propagating normally from ($-z$) direction. The refractive index of PDMS is set to 1.4 and that of gold is taken from the Johnson and Christy database.[33] The extinction cross sections are calculated for all displacement

Table 1. Mechanical properties of PDMS and gold.

Parameters	Notation	PDMS	Gold
Poisson ratio	ν	0.49	0.44
Lamé parameter (N m^{-2})	μ	667×10^3	—
Bulk modulus (Pa)	κ	3.333×10^7	—
Young's modulus (Pa)	E	750×10^3	70×10^9
Density (kg m^{-3})	ρ	971	19300

values for a wavelength range from 600 to 1100 nm using the formula:

$$\sigma_{ext} = \frac{-\omega\varepsilon_0}{2}\Im\left(\int_v E_i^*.P\, dv\right)/I_0 \quad (1)$$

where ω is the angular frequency; ε_0 is the vacuum permittivity; E_i is the incident electric field; P is defined as $(\varepsilon(\omega) - \varepsilon_m)E_{tot}$ (with $\varepsilon(\omega)$ the relative permittivity of the gold, ε_m the relative permittivity of the surrounding medium, and E_{tot} the total electric field); I_0 represents the irradiance determined as $I_0 = \frac{1}{2}|E_0|^2\sqrt{\varepsilon_m}\sqrt{\frac{\varepsilon_0}{\mu_0}}$ (with E_0 the amplitude of the incident electric field and μ_0 the vacuum permeability); v is the volume of the NPs.

3. Results and Discussion

3.1. Mechanical Simulations

Several parameters may influence the interparticle distance when the PDMS membrane, which supports them, is under stretching. The effects of the dimensions of the PDMS membrane, as well as the shape and size of the AuNPs, are numerically investigated in this section.

3.1.1. Effects of the PDMS Membrane Dimensions on the Gap Evolution

The rate of change of the interparticle gap in respect to the applied deformation represented by the normalized relative gap variation (NRGV), defined as $\Delta g/(g_0\varepsilon) = (g - g_0)/(g_0\varepsilon)$ with g denoting the gap after stretching and ε representing the extension applied to the PDMS membrane, has been calculated in the case of the disks dimer system under different values of displacement ranging from 0% to 20%. The parameters R and L are set to 90 and 2000 nm, respectively. The PDMS thickness varies from 100 to 4000 nm, with a step of 100 nm. **Figure 2**a shows the evolution of the NRGV as a function of the membrane thickness for several values of ε. It can be observed that the NRGV increases rapidly as the PDMS thickness grows from 100 to 500 nm, and subsequently approaches a saturation value, which would be reached for thicknesses beyond the ranges of values accessible in the simulation. This nonlinear behavior was observed for all ε values. Beyond $H = 1000$ nm, the effect of the thickness of the membrane can be considered negligible. The non-superimposition of the curves can be attributed to the fact that the PDMS is modeled as a hyperelastic material, yielding a nonlinear response of the NRGV as a function of the applied strain, which can be observed in the inset. With an elastic model, all these curves should overlap as the variation of the gap should be proportional to ε. A striking result is that the interparticle gap is much more stretched than the PDMS membrane, by a percentage up to 144%. This demonstrates that a simple model where the gap deformation is equal to the applied deformation is largely unrealistic.

To quantify the local length variation in the PDMS, the displacement gradient (du/dx where u is the component of the displacement field along x direction) is plotted in Figures 2c and 2d, respectively, for $H = 100$ nm and $H = 300$ nm, for an applied stretching of $\varepsilon = 20\%$. One can find that the AuNPs move with the stretched membrane without undergoing any noticeable change in their initial shapes. This is attributed to their higher Young's modulus compared to PDMS, which makes them resistant to the applied deformations. Additionally, the presence of the AuNPs induces a local stiffness of the PDMS in the contact region below the particles. The same effect was experimentally observed in a PDMS film coated with silica NPs.[34] It is interesting to observe that this stiffened region is on the order of the PDMS thickness for small thickness values ($H = 100$ nm), which makes the membrane resistant to the x-deformation within this region. As a result, the interparticle gap experiences less stretching. For large H values ($H = 300$ nm), the influence of the NPs (stiffness) becomes negligible when moving away in the z-direction. This allows the region along the bottom interface to freely deform in the x-direction, resulting in more compression in transverse directions. Consequently, a curved and enhanced gap is observed. The computed displacement gradient along a line passing through the center of the nanoparticle (Figure 2b) further confirms that the characteristic thickness at which the PDMS is significantly affected by the NPs is approximately 100 nm.

On the other hand, the PDMS length shows no noticeable impact on the NRGV, when it is varying from 1 to 10 μm (see Figure S1a, Supporting Information). This behavior can be attributed to the characteristic length at which the PDMS is influenced (stiffness) by the presence of NPs. This length is on the order of 250 nm (Figure S1b, Supporting Information), which is smaller than the range of the lengths considered in this study.

3.2. Effects of the Particle Size and Shape on the Gap Evolution

Two systems, a disks dimer and a squares dimer, are investigated. The PDMS membrane has a fixed thickness $H = 300$ nm and length $L = 1000$ nm. For comparison purposes, the disk (R) and the square ($l_s = \sqrt{\pi}R$) are chosen to have the same contact area with the PDMS membrane. The NRGV has been calculated for an increasing radius (R) ranging from 90 to 150 nm, with the applied deformation fixed at 20% (see **Figure 3**a). When the contact area increases, in both cases, the NRGV also increases, showing a linear behavior in both systems.

In order to understand the impact of the NP size on the gap, we introduce a simple model involving a dimer of nanoparticles (with radius [R]) deposited on a stretchable film as sketched in Figure 3b. This model considers only the displacement of the NPs in the x-direction (uniaxial stretching) and does not take into account the real shape of AuNPs. The x-coordinates of the nanoparticle center at rest (x_0) and after stretching (x_1) are determined as:

$$x_0 = \frac{g_0}{2} + R \quad (2)$$

$$x_1 = \frac{g}{2} + R \quad (3)$$

and related by $x_1 = x_0(\varepsilon + 1)$. From this set of equations, we obtain the NRGV defined as a function of the nanoparticle radius: $\frac{\Delta g}{g_0\varepsilon} = 1 + \frac{2R}{g_0}$. The computed NRGV using this basic model (represented by the black curve in Figure 3a) demonstrates a similar effect of nanoparticle size on the gap compared to the hyperelastic model.

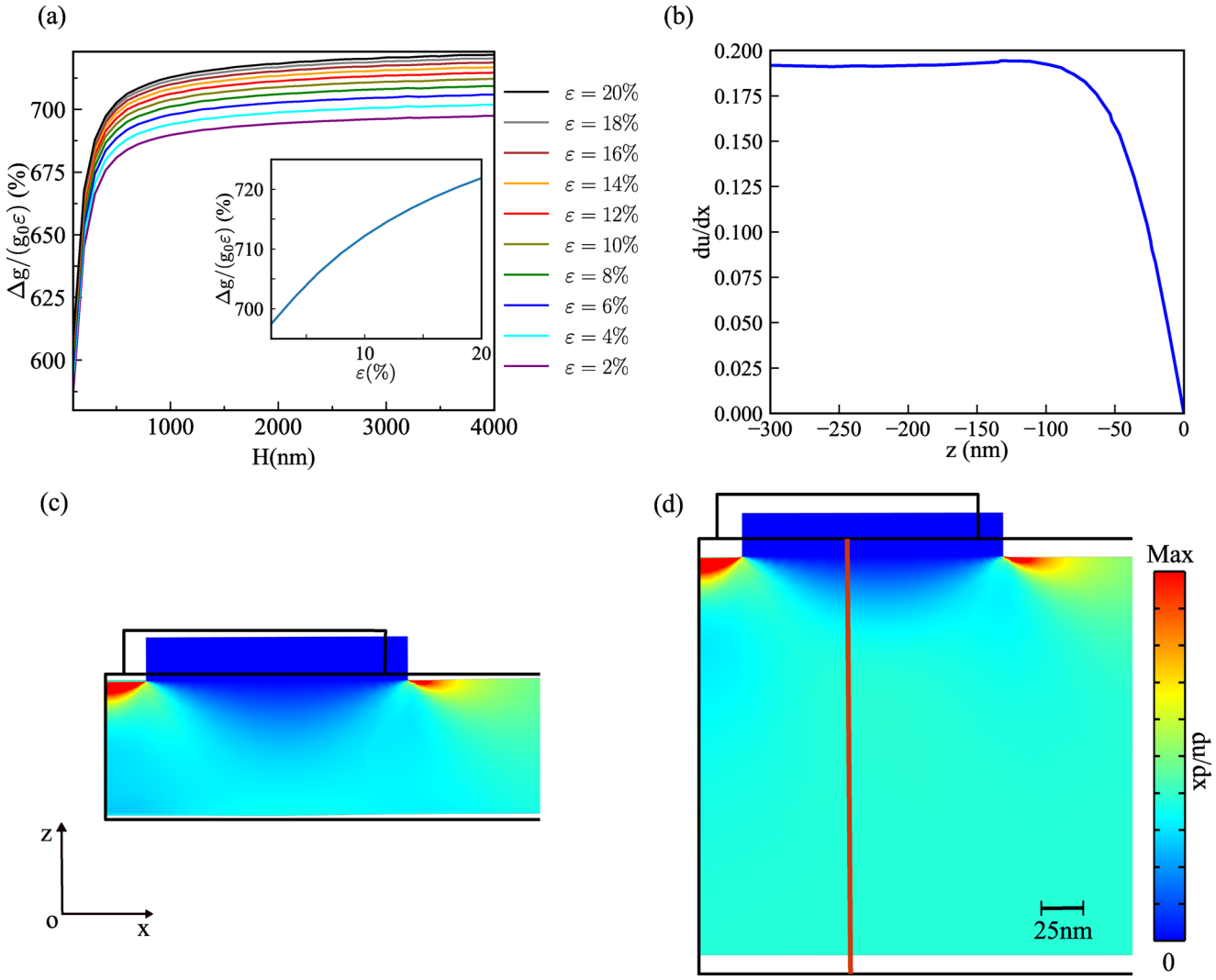

Figure 2. a) Normalized relative gap variation as a function of the PDMS thickness. Inset: normalized relative gap variation as a function of the applied displacements for $H = 4000$ nm; b) computed displacement gradient along a line passing through the nanodisk center in the z-direction (red line in (d)); c) x–z view of the displacement gradient maps of the system under 20% of displacement for $H = 100$ nm; d) same as (c) for $H = 300$ nm. Solid black lines in (c) and (d) correspond to the initial positions at rest, whereas the displacement gradient is plotted on the deformed geometry.

Moreover, it was found that the NRGV is larger in the case of a disks dimer than in one of the squares dimer. This distinction could be understood from the shape of the stiffened contact zone of the PDMS with the NPs. Intuitively, the area of this zone within the gap region is smaller in the disks dimer case allowing the membrane to be stretched more in the x-direction. As a result, a more enhanced gap is observed compared to the case of the squares dimer (see Figure 3c,d).

A disk–square system (with the following dimensions: R= 90 nm, $l_s = \sqrt{\pi}90$ nm, and $g_0 = 10$ nm) was also studied (see Figure S2, Supporting Information). It can be clearly observed that the NRGV is smaller than that obtained in the disks dimer system and larger than the squares dimer, which is in agreement with the proposed assumptions above, since the area in the gap region is in between the two previous cases. Moreover, it was found that the interparticle distances are such that the NRGV is much larger than 100%, which means that the gap increase is much larger than if it is supposed that the particles exhibit the same displacement percentage as the applied one.

3.3. Opto-Mechanical Simulations

After studying and understanding how the geometrical parameters of the system and the applied displacements affect the evolution of the interparticle gap, we investigate the evolution of the plasmonic response of the metallic nanostructures, excited by a monochromatic plane wave (for a wavelength range 600–1100 nm) linearly polarized along the x-direction, when the membrane is stretched along the x-axis from 0% to 20%. The PDMS thickness is set at 300 nm for all plasmomechanical devices in order to reduce the required computational time and memory. **Figure 4**a represents the evolution of the

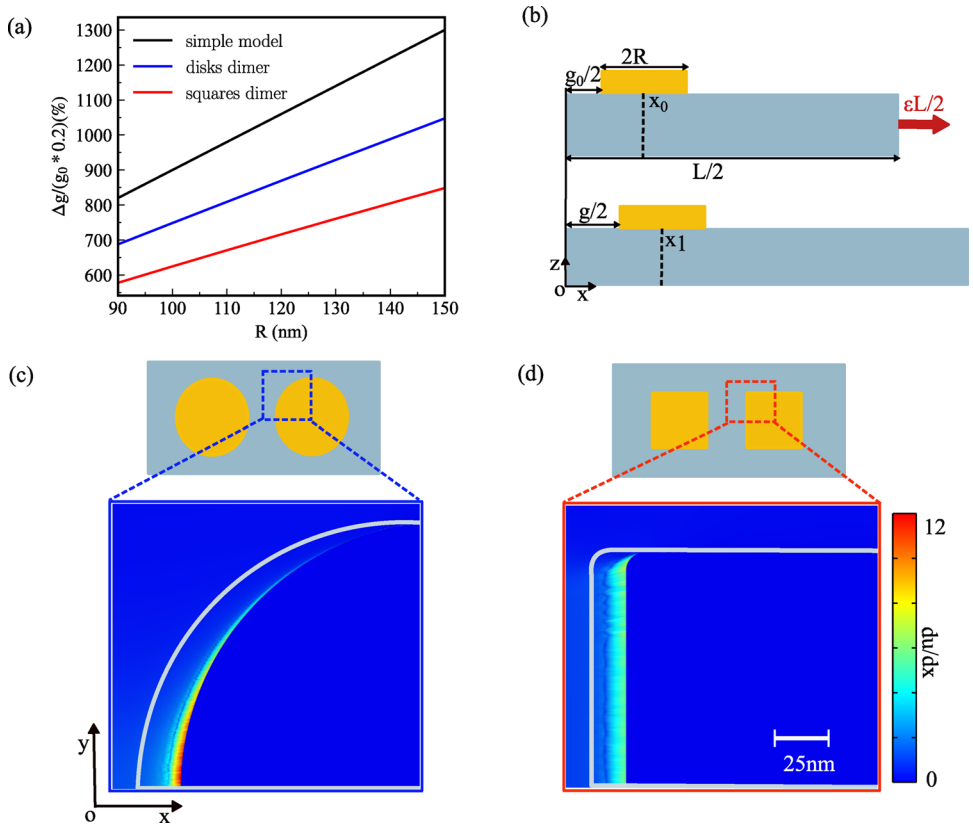

Figure 3. a) Normalized relative gap variation as a function of the particle size for the disks and the squares dimer; b) sketch to illustrate the nanoparticle displacement with PDMS deformation; c) *x*–*y* view of the displacement gradient maps of the system under 20% of displacement for the disks dimer (*R* = 150 nm); d) same as (c) for the squares dimer. Solid white lines in (c) and (d) correspond to the initial positions at rest.

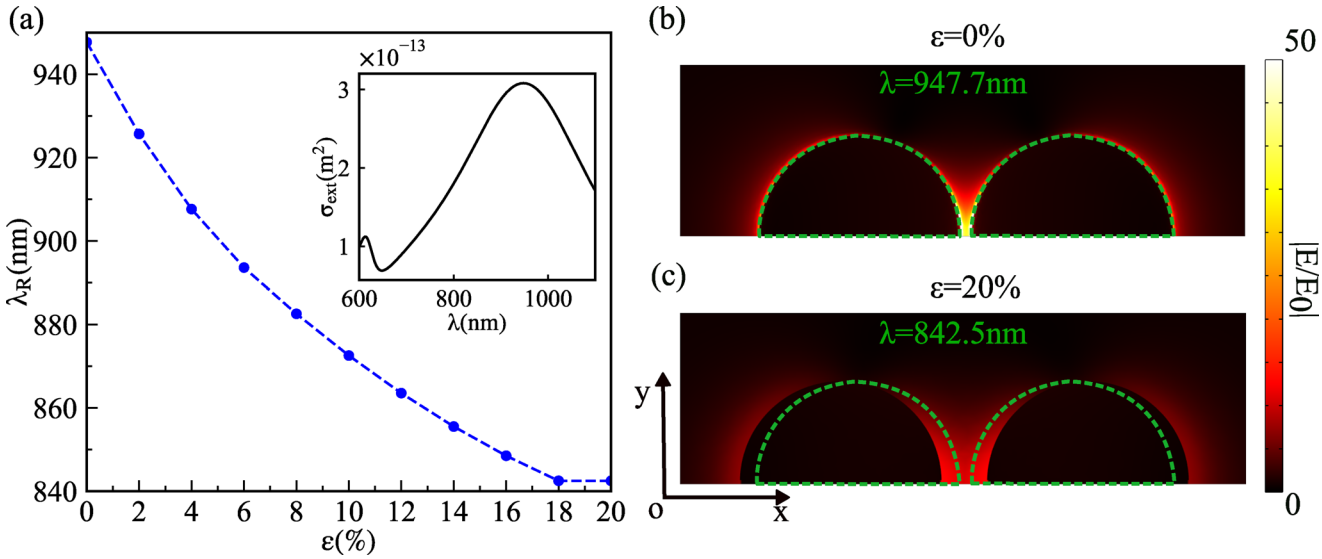

Figure 4. a) Calculated evolution of the plasmonic resonance wavelength for the disks dimer as a function of the applied displacement ranging from 0% to 20%. Inset: extinction spectrum obtained at $\varepsilon = 0\%$. b) Electric field distribution of the structure at rest; c) same as for (b) under 20% of displacement.

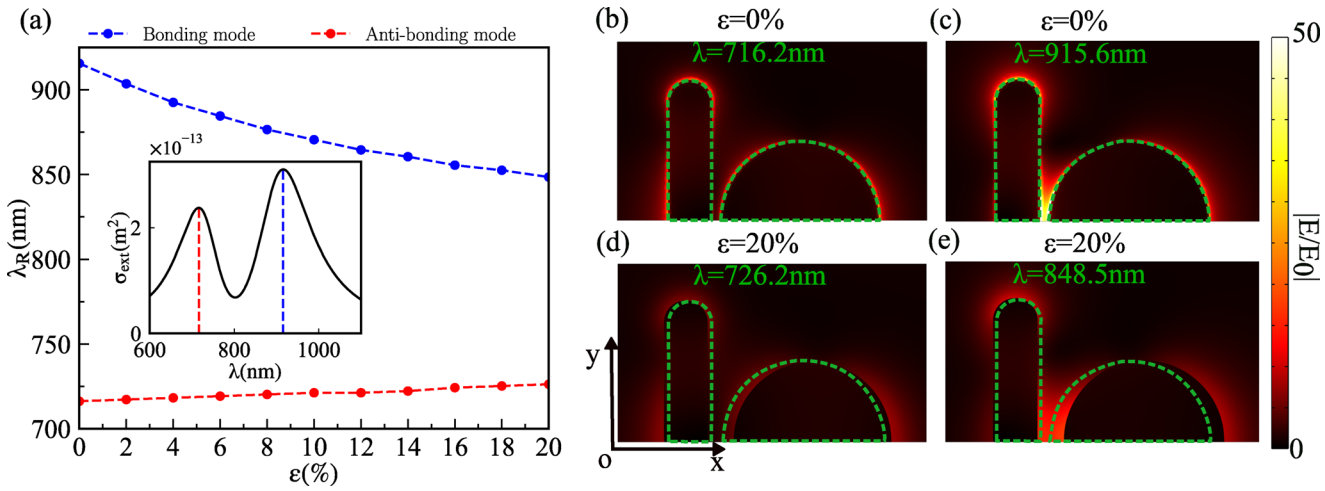

Figure 5. a) Calculated evolution of the resonance wavelength as a function of the applied displacement ranging from 0% to 20% for the disk–rod dimer; electric field amplitude distribution of the structure at rest and under 20% of displacement: for the antibonding mode (b,d), and for the bonding mode (c,e).

plasmonic resonance wavelength, obtained for a disks dimer system (with $R = 90$ nm and $g_0 = 10$ nm), as a function of the applied displacements. The inset represents the extinction cross section spectrum obtained at $\varepsilon = 0\%$. The main broad peak observed in the inset at $\lambda = 947.7$ nm is the bonding mode, which results from the low-frequency and antisymmetric combination between the plasmonic dipolar modes of the disks. It is important to note that the symmetric mode cannot be excited when employing a monochromatic plane wave. The results show that the resonance wavelength exhibits a nonlinear blueshift of 105.2 nm when the applied displacement is increased from 0% to 20%.

At rest position, the field is localized and enhanced in the gap region. The resonance frequency of the antisymmetric mode is lowered due to the attractive potential between charges of opposite signs located on each side of the gap. With increasing strains, the interparticle gap becomes larger ($\frac{\Delta g}{g_0}(0\% \rightarrow 20\%) = 3.1$), the field confinement becomes lower, and the frequency increases due to lower attractive potential experienced by the charges localized in the gap region.[35] Figure 4b,c clearly evidences the strong decrease of the near-field enhancement in the gap region at plasmon resonance, indicating that the AuNPs are almost isolated for $\varepsilon = 20\%$ compared to $\varepsilon = 0\%$.

Under the same optical and mechanical conditions, the squares dimer and the disk–square dimer, illustrated in Figures 1c and 1d, respectively, have been studied (with $l_s \approx 159.5$ nm, $R = 90$ nm, and $g_0 = 10$ nm). The evolution of the resonance wavelength as a function of the applied displacement ranging from 0% to 20% (See Figure S3a,b, Supporting Information) shows the same behavior as in the case of the disks dimer. The resonance peak is blueshifted by 119.2 nm for the squares dimer and by 103.2 nm for the disk–square dimer as the strain passes from 0% to 20%.

Let us now consider another plasmomechanical system able to generate Fano resonance. The proposed structure is schematically presented in Figure 1e with the following dimensions: $l_r = 320$ nm, $w = 50$ nm and $R = 90$ nm. **Figure 5**a represents the evolution of the resonance maxima as a function of the applied displacements, with the inset showing the FR at $\varepsilon = 0\%$. The bright dipolar mode of the disk, which can be easily excited by a monochromatic planewave, can couple to the first dark mode of the rod, which cannot be directly excited by a planewave. When the AuNPs are close enough to each other (about 10 nm), strong coupling occurs and these modes hybridize, leading to the formation of bonding and antibonding modes whose interference is at the origin of a Fano resonance profile.[10] When the displacement percentage passes from 0% to 20%, the bonding mode (long wavelength maximum) exhibits a strong blue shift of 67.1 nm while the antibonding mode shows a smaller shift in the opposite direction, of 10 nm. In fact, the dramatic amplification of the gap ($\frac{\Delta g}{g_0}(0\% \rightarrow 20\%) = 1.98$), when the PDMS is under stretching, causes a decoupling and a transition to weak interaction between the two modes as demonstrated in **Figure 6**b, where the absorption cross section spectrum show a single peak at $\varepsilon = 20\%$ (for more details, see ref. [10]). The normalized electric field ($|E/E_0|$) maps depicted in Figure 5 are taken at the extinction maxima of the bonding (low frequency, Figure 5c–e) and the antibonding (high frequency, Figure 5b–d) modes at $\varepsilon = 0\%$ and $\varepsilon = 20\%$. When the structure is at rest, it can be observed that the electric field is strongly enhanced and confined in the gap zone for the bonding mode, while it exhibits negligible values for the antibonding mode in this region. As the applied displacement increases up to 20%, the electric field amplitude, particularly in the bonding mode, decreases significantly in the gap region as a consequence of the AuNP decoupling. It is also possible to see that the disk particle experiences more displacement than the rod, which confirms the previous findings in the mechanical study in the case of the disk–square dimer.

Here, the strain sensitivity, defined as the resonant wavelength shift divided by the strain variation is calculated using $\Delta\lambda/\Delta\varepsilon$ instead of $d\lambda/d\varepsilon$, since we take into account the reference geometry at $\varepsilon = 0\%$ and the final deformed geometry to quantify the average sensitivity and not the instantaneous sensitivity at a specific point. Figure 6a depicts the strain sensitivity of the four investigated systems. It can be clearly observed that the disks dimer

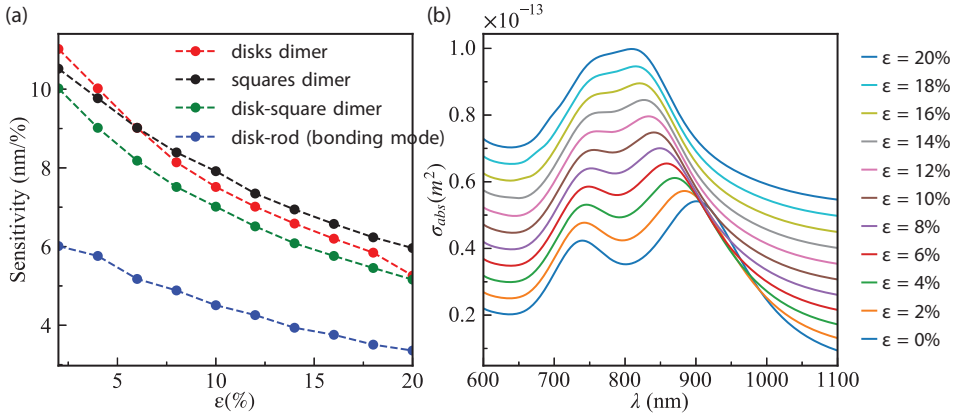

Figure 6. a) Strain sensitivity variation of all the investigated devices as a function of the applied displacement; b) absorption cross sections of the disk-rod dimer for all displacement values.

and the squares dimer exhibit the highest sensitivity, decreasing from 11 nm/% (small stretching) to 5.26 nm/% (large stretching) and from 10.52 nm/% to 5.96 nm/%, respectively. On the other hand, the lowest sensitivity is obtained in the case of the disk–rod dimer, decreasing from 6 nm/% to 3.35 nm/% for the bonding mode, while the antibonding mode is almost insensitive to the applied deformation.

The sensitivities achieved in this study, in all cases, are much higher than those obtained in a similar system of bow tie nanoantennas (1.9 nm/%).[23] Nevertheless, the sensitivity does not provide information on the ability of strain sensors to detect and distinguish color changes and, thus, their performances. For this reason, a more specific parameter is calculated: the figure of merit (FOM), defined as the ratio of the strain sensitivity to the full width at half maximum (FWHM). In contrast to sensitivity, which is larger in the case of the LSPR-based systems compared to the disk–rod dimer, the highest FOM (**Figure 7**) is obtained for the disk–rod dimer, from 0.039%$^{-1}$ down to 0.022%$^{-1}$ as the applied displacement passes from 0% to 20%. This behavior can be attributed to the narrow FWHM of the Fano resonance.

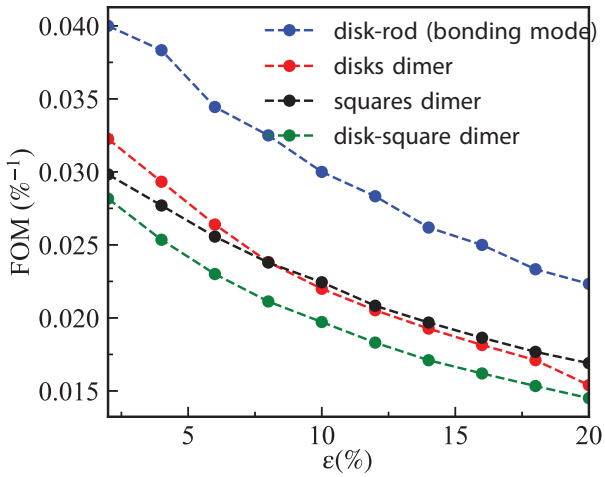

Figure 7. FOM variation of all the investigated devices as a function of the applied displacement.

Figure 8 depicts the extinction cross section spectra of our structure at rest and under 20% of stretching. In the last case, two scenarios are considered: the basic model, in which the particles move away from each other at the same percentage as the macroscopic applied strain, which is adopted by some works,[18] and nonlinear evolution (hyperelastic model), as demonstrated in the presented work. As we can see, the bonding mode is blueshifted by 14 nm in the basic model, which is smaller compared with our results ($\Delta\lambda = 67.1$ nm) by a factor of 4.8, whereas the antibonding mode position remains mostly unaltered.

4. Conclusion

In this work, various plasmomechanical devices are numerically investigated. The influence of geometrical parameters of the system on the interparticle gap when the flexible membrane is

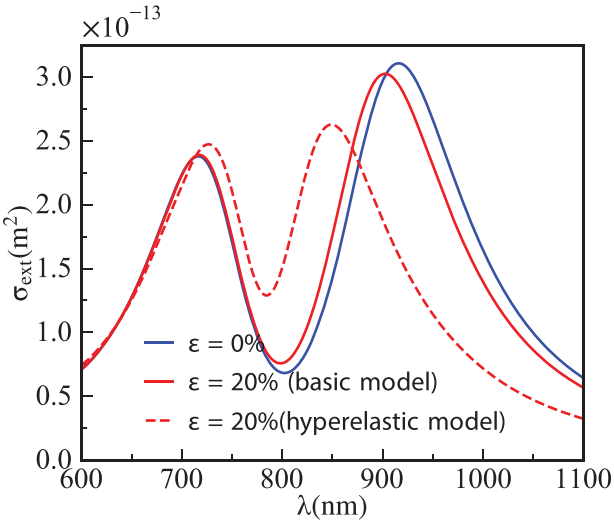

Figure 8. Extinction cross section spectrum obtained at the rest state (blue curve) and at the maximum applied displacement (red curves: the dashed one corresponds to the case where the gap amplifies by the same percentage as the macroscopic applied displacement and the solid one is the nonelastic case where it undergoes higher amplification).

stretched was investigated through a fully mechanical study. The obtained results reveal that the gap is significantly affected by the membrane thickness, and the NRGV is found to rapidly increase for small H values up to 720%. Beyond $H = 1000$ nm, the NRGV approaches a saturation value which has been attributed to a novel effect described in this study: the stiffness of PDMS near the non-deformable AuNPs. As a result, the deformation is transferred to the gap and amplified to compensate for this effect beneath the AuNPs. Additionally, it was observed that the NRGV exhibits a linear increase with the size of the AuNPs and is affected by their shape due to the shape of the stiffened contact area. Then, an optomechanical study was performed. In fact, the dramatic amplification of the gap results in a large plasmonic resonance shift of the disk–rod and the disks dimers compared to a basic model where the gap is supposed to evolve with the same percentage as the macroscopic deformation. The sensitivity of the low-frequency dipole mode of the disks dimer is determined to be 5.26 nm per 1% strain variation, higher than that for the bonding mode of the disk–rod dimer (3.35 nm per 1%) for 20% of deformation. These sensitivities are much larger than those of the previously reported plasmomechanical system of a bow tie nanoantenna. Although the disk–rod dimer exhibits lower strain sensitivity than the disks dimer, due to its narrower linewidth, it provides the highest FOM (from $0.039\%^{-1}$ down to $0.022\%^{-1}$), which makes it a preferred candidate in strain-sensing applications. These findings are of great interest in understanding the optical response of plasmomechanical systems under stretching and in designing more efficient devices by controlling the shape and interaction of closely coupled NPs.

Supporting Information

Supporting Information is available from the Wiley Online Library or from the author.

Acknowledgements

This work was supported by the Agence Nationale de la Recherche and the FEDER (INSOMNIA project, contract "ANR-18-CE09-0003") and by the Graduate School NANO-PHOT (École Universitaire de Recherche, contract ANR-18-EURE-0013). Financial support of NanoMat (www.nanomat.eu) by the "Ministère de l'enseignement supérieur et de la recherche," the "Conseil régional Champagne-Ardenne," the "Fonds Européen de Développement Régional (FEDER)," and the "Conseil général de l'Aube" is also acknowledged.

Conflict of Interest

The authors declare no conflict of interest.

Data Availability Statement

Research data are not shared.

Keywords

hyperelasticity, plasmomechanics, sensing, strong coupling

Received: July 5, 2023
Revised: July 29, 2023
Published online:

[1] O. Saison-Francioso, G. Leveque, R. Boukherroub, S. Szunerits, A. Akjouj, *J. Phys. Chem. C* **2015**, *119*, 28551.
[2] G. Baffou, R. Quidant, C. Girard, *Appl. Phys. Lett.* **2009**, *94*, 15.
[3] A. Alabastri, M. Malerba, E. Calandrini, A. Manjavacas, F. De Angelis, A. Toma, R. Proietti Zaccaria, *Nano Lett.* **2017**, *17*, 5472.
[4] Y. Zhao, Y. Luo, S. Wu, C. Wang, N. Ahmidayi, G. Lévêque, X. Portier, T. Xu, *Phys. E* **2023**, *146*, 115534.
[5] T. Xu, Y. Luo, S. Wu, B. Deng, S. Chen, Y. Zhong, S. Wang, G. Lévêque, R. Bachelot, F. Zhu, *Adv. Sci.* **2022**, *9*, 2202150.
[6] C. Bravin, V. Amendola, *ACS Appl. Nano Mater.* **2021**, *5*, 578.
[7] A. Shiohara, J. Langer, L. Polavarapu, L. M. Liz-Marzán, *Nanoscale* **2014**, *6*, 9817.
[8] S. A. Maier, *Plasmonics: Fundamentals and Applications*, vol. *1*, Springer, Berlin **2007**.
[9] V. Amendola, R. Pilot, M. Frasconi, O. M. Maragò, M. A. Iatì, *J. Phys.: Condens. Matter* **2017**, *29*, 203002.
[10] D. Eschimèse, F. Vaurette, C. Ha, S. Arscott, T. Mélin, G. Lévêque, *Nanoscale Adv.* **2022**, *4*, 1173.
[11] P. K. Jain, M. A. El-Sayed, *Chem. Phys. Lett.* **2010**, *487*, 153.
[12] A. Christ, G. Lévêque, O. Martin, T. Zentgraf, J. Kuhl, C. Bauer, H. Giessen, S. Tikhodeev, *J. Microsc.* **2008**, *229*, 344.
[13] P. K. Jain, W. Huang, M. A. El-Sayed, *Nano Lett.* **2007**, *7*, 2080.
[14] T. Maurer, J. Marae-Djouda, U. Cataldi, A. Gontier, G. Montay, Y. Madi, B. Panicaud, D. Macias, P.-M. Adam, G. Lévêque, T. Bürgi, R. Caputo, *Front. Mater. Sci.* **2015**, *9*, 170.
[15] A. Mizuno, A. Ono, *ACS Appl. Nano Mater.* **2021**, *4*, 9721.
[16] A. Paghi, M. Corsi, S. Corso, S. Mariani, G. Barillaro, *Nanoscale Horiz.* **2022**, *7*, 425.
[17] G. Emanuele Lio, A. De Luca, C. P. Umeton, R. Caputo, *J. Appl. Phys.* **2020**, *128*, 093107.
[18] G. E. Lio, G. Palermo, R. Caputo, A. De Luca, *J. Appl. Phys.* **2019**, *125*, 082533.
[19] G. E. Lio, G. Palermo, A. De Luca, R. Caputo, *J. Chem. Phys.* **2019**, *151*, 24.
[20] J. Marae-Djouda, A. Gontier, R. Caputo, G. Lévêque, B. Bercu, Y. Madi, G. Montay, P.-M. Adam, M. Molinari, S. Stagon, T. Maurer, *ACS Appl. Nano Mater.* **2018**, *1*, 2347.
[21] P. Jia, D. Kong, H. Ebendorff-Heidepriem, *ACS Appl. Nano Mater.* **2020**, *3*, 8242.
[22] A. Kakati, S. Das, in *2018 IEEE Sensors*, IEEE, Piscataway, NJ **2018**, pp. 1–4.
[23] F. Laible, D. A. Gollmer, S. Dickreuter, D. P. Kern, M. Fleischer, *Nanoscale* **2018**, *10*, 14915.
[24] Z. Buch, S. Schmid, *Opt. Express* **2022**, *30*, 5294.
[25] G. Palermo, U. Cataldi, A. Condello, R. Caputo, T. Bürgi, C. Umeton, A. De Luca, *Nanoscale* **2018**, *10*, 16556.
[26] F. Lütolf, D. Casari, B. Gallinet, *Adv. Opt. Mater.* **2016**, *4*, 715.
[27] N. Verellen, P. Van Dorpe, C. Huang, K. Lodewijks, G. A. Vandenbosch, L. Lagae, V. V. Moshchalkov, *Nano Lett.* **2011**, *11*, 391.
[28] S. Zhang, L. Chen, Y. Huang, H. Xu, *Nanoscale* **2013**, *5*, 6985.
[29] Z.-J. Yang, Z.-S. Zhang, Z.-H. Hao, Q.-Q. Wang, *Appl. Phys. Lett.* **2011**, *99*, 081107.
[30] J.-N. He, J.-Q. Wang, P. Ding, C.-Z. Fan, L. R. Arnaut, E.-J. Liang, *Plasmonics* **2015**, *10*, 1115.
[31] J. Briones, W. Espulgar, S. Koyama, H. Takamatsu, E. Tamiya, M. Saito, *Sci. Rep.* **2021**, *11*, 12995.
[32] H. Peussa, J. Kreutzer, E. Mäntylä, A.-J. Mäki, S. Nymark, P. Kallio, T. O. Ihalainen, *PLoS ONE* **2022**, *17*, e0268570.
[33] P. B. Johnson, R.-W. Christy, *Phys. Rev. B* **1972**, *6*, 4370.
[34] H. Huang, I. Dobryden, P.-A. Thorén, L. Ejenstam, J. Pan, M. Fielden, D. Haviland, P. M. Claesson, *Compos. Sci. Technol.* **2017**, *150*, 111.
[35] W. Rechberger, A. Hohenau, A. Leitner, J. Krenn, B. Lamprecht, F. Aussenegg, *Opt. Commun.* **2003**, *220*, 137.